



Published in final edited form as:

Lab Invest. 2012 October ; 92(10): 1492–1502. doi:10.1038/labinvest.2012.109.

## Multicolored Stain-free Histopathology with Coherent Raman Imaging

Christian W. Freudiger<sup>1</sup>, Rolf Pfanni<sup>2</sup>, Daniel A. Orringer<sup>3,4,5</sup>, Brian G. Saar<sup>1,†</sup>, Minbiao Ji<sup>1</sup>, Qing Zeng<sup>6,7</sup>, Linda Ottoboni<sup>8</sup>, Wei Ying<sup>9</sup>, Christian Waeber<sup>9</sup>, John. R. Sims<sup>9</sup>, Philip L. De Jager<sup>8,10,11</sup>, Oren Sagher<sup>5</sup>, Martin A. Philbert<sup>12</sup>, Xiaoyin Xu<sup>6,7</sup>, Santosh Kesari<sup>13,14</sup>, X. Sunney Xie<sup>1</sup>, and Geoffrey S. Young<sup>6,7,\*</sup>

<sup>1</sup>Department of Chemistry and Chemical Biology, Harvard University, Cambridge (MA)

<sup>2</sup>Department of Pathology and Laboratory Medicine, Tufts Medical Center, Boston (MA)

<sup>3</sup>Department of Neurosurgery, Brigham and Women's Hospital, Boston (MA)

<sup>4</sup>Department of Neurosurgery, Harvard Medical School, Boston (MA)

<sup>5</sup>Department of Neurosurgery, University of Michigan Medical School, Ann Arbor (MI)

<sup>6</sup>Department of Radiology, Brigham and Women's Hospital, Boston (MA)

<sup>7</sup>Department of Radiology, Harvard Medical School, Boston (MA)

<sup>8</sup>Department of Neurology, Brigham and Women's Hospital, Boston (MA)

<sup>9</sup>Department of Radiology, Massachusetts General Hospital, Charlestown (MA)

<sup>10</sup>Department of Neurology, Harvard Medical School, Boston (MA)

<sup>11</sup>Broad Institute of Harvard University and MIT, Boston (MA)

<sup>12</sup>Department of Environmental and Health Sciences, University of Michigan, Ann Arbor (MI)

<sup>13</sup>Department of Medical Oncology, Dana-Farber Cancer Institute, Boston (MA)

<sup>14</sup>Department of Neuroscience, Moores Cancer Center, University of California at San Diego, San Diego (CA)

### Abstract

Conventional histopathology with hematoxylin & eosin (H&E) has been the gold standard for histopathological diagnosis of a wide range of diseases. However, it is not performed *in vivo* and requires thin tissue sections obtained after tissue biopsy, which carries risk, particularly in the central nervous system. Here we describe the development of an alternative, multicolored way to visualize tissue in real time through the use of coherent Raman imaging (CRI), without the use of

---

Users may view, print, copy, download and text and data- mine the content in such documents, for the purposes of academic research, subject always to the full Conditions of use: [http://www.nature.com/authors/editorial\\_policies/license.html#terms](http://www.nature.com/authors/editorial_policies/license.html#terms)

Correspondence: gsyoun@partners.org.

<sup>†</sup>Present address: MIT Lincoln Laboratory, Lexington (MA)

**Disclosure of Competing Interest:** Harvard University has filed a patent application based on coherent Raman imaging instrumentation.

dyes. CRI relies on intrinsic chemical contrast based on vibrational properties of molecules and intrinsic optical sectioning by nonlinear excitation. We demonstrate that multi-color images originating from CH<sub>2</sub> and CH<sub>3</sub> vibrations of lipids and protein, as well as two-photon absorption of hemoglobin, can be obtained with subcellular resolution from fresh tissue. These stain-free histopathological images show resolutions similar to those obtained by conventional techniques, but do not require tissue fixation, sectioning or staining of the tissue analyzed.

## Keywords

Coherent anti-Stokes Raman scattering; CARS; Histology; *In vivo* microscopy; Stimulated Raman scattering; SRS

---

## Introduction

With rare exceptions, histopathological techniques cannot be used for *in situ* diagnosis since they require the tissue to be frozen or fixed, thinly sliced, and stained with devitalizing dyes before the tissue can be observed under a microscope. A real-time, *in situ* technique for acquiring histopathological images would thus be tremendously advantageous in situations where the tissue removal imposes risk and delay required for fixation, sectioning and staining. Ideally, *in situ* stain-free histopathology could be used in the setting of tumor surgery to examine the margins of a resection cavity for residual neoplastic tissue.

Coherent Raman imaging (CRI), including coherent anti-Stokes Raman scattering (CARS) microscopy<sup>1,2</sup> and stimulated Raman scattering (SRS) microscopy<sup>3-6</sup>, allows chemical imaging based on intrinsic vibrational properties of the molecules in the tissue and thus does not require staining or labeling. The more recent SRS microscopy techniques offer further advantages: (1) elimination of image artifacts due to non-resonant background, (2) excitation spectra identical to well-documented spontaneous Raman spectra, (3) a linear relationship between signal and concentration of target molecules. Compared to spontaneous Raman scattering, signal levels are amplified by orders of magnitude by virtue of stimulated excitation of molecular vibrations, allowing video-rate image acquisition speeds<sup>7,8</sup>. Due to nonlinear excitation, CRI enables intrinsically three-dimensional sectioning<sup>1,4,9</sup> and does not require physical sectioning of the tissue. Efficient signal detection in reflection of thick samples<sup>8,10</sup> as well as biocompatibility of laser excitation intensities<sup>11,12</sup> have been demonstrated, allowing stain-free, *in vivo* imaging in mice<sup>7,8,13-16</sup> and humans<sup>8,17</sup>.

The properties of CRI have inspired us<sup>18</sup> and others<sup>19-21</sup> to image diseases with CARS microscopy and development of miniaturized clinical instrumentation is underway<sup>22-25</sup>. This work describes the development of multicolor SRS imaging with contrast originating from lipids, protein and red blood cells, aiming to resemble the most widely used stain in histopathology, hematoxylin and eosin (H&E). We demonstrate *ex vivo* that the key diagnostic features appreciated with H&E staining are well visualized with CRI in tissue from wild type mice as well as mouse models of various diseases of the central nervous system.

## Materials and Methods

### Imaging Setup and Processing

CRI requires two synchronized pulse trains to achieve stimulated excitation of the vibrational transition. In narrowband SRS, the frequency bandwidth of such lasers is chosen to be smaller than the typical linewidth of Raman transition and the difference in frequency of the two center frequencies can be tuned to excite a single vibration at a time. Compared to multiplex excitation of multiple vibrations simultaneously using broadband lasers, this approach maximizes imaging speed. We use a passively mode-locked Nd:YVO<sub>4</sub> laser (PicoTrain, High Q Laser) at 1064nm (7ps pulse-duration, 76MHz repetition rate) to provide the first beam, known as the Stokes beam. A portion of this beam is frequency-doubled and used to pump an optical parametric oscillator (Levante Emerald, APE GmbH) to provide the second tunable beam (650nm-1000nm tuning range), known as the pump beam. The two pulse trains are then overlapped in space and time, aligned into a laser scanning microscope (FV300, Olympus) and focused into the sample with a high numerical aperture (NA) water-immersion lens (UPlanSApo 60×, Olympus)<sup>2,4</sup>.

For SRS microscopy we measure the intensity loss of the pump beam due the excitation of molecular vibrations in the focus. Sensitive detection of the signal requires the implementation of a high-frequency modulation transfer scheme to distinguish the SRS signal from linear sample absorption or laser intensity fluctuation. This relies on the fact that SRS can only occur if both pump and Stokes are incident on the sample. By modulating the Stokes beam at a known frequency with an acousto-optic modulator and measuring the modulation transfer to the originally un-modulated pump beam at the same frequency, SRS can be detected specifically. If the modulation frequency is faster than the typical laser noise (e.g. 10MHz), high sensitivity detection is achieved at the moderate laser power required for medical imaging. Experimentally, the transmitted light from the sample is collected with a high NA oil condenser (Nikon), filtered to block the modulated Stokes beam (CARS890/220, Chroma) and detected with a large-area photodiode (FDS1010, Thorlabs). The modulation transfer is measured by a lock-in amplifier (SR844, Stanford Research), whose signal is fed into the microscope to provide the signal for a pixel. All images were sampled with 512 × 512 pixels ~30μs pixel dwell time, which is limited by the speed of the lock-in amplifier. In the meantime we have developed improved detection electronics and achieved imaging speeds up to video-rate (30 frames per second)<sup>4,8</sup>.

For the multi-color imaging, three individual scans per region in the tissue are acquired with one beam fixed at 1064nm and the other at 816.7nm (CH<sub>2</sub>-stretching vibration), 810.5nm (CH<sub>3</sub>-stretching vibration) and 700nm (hemoglobin TPA). Fast tuning between these three wavelengths can be achieved within a few seconds by changing the Lyot filter and the cavity length of the optical parametric oscillator. Images are acquired with the microscope scanning software and processed in ImageJ. Pseudo-colors can be assigned arbitrarily, e.g. to mimic H&E stained sections. In most cases we use a red-green-blue (RGB) look-up table. The green and red channels show CH<sub>2</sub> and hemoglobin images, respectively. The blue channel is a CH<sub>3</sub>-CH<sub>2</sub> difference image thresholded to show only nuclei (see Results section). To normalize for the curvature of the field of view we calculated a featureless

reference image by averaging and smoothing about one hundred SRS images acquired the same day from different regions and dividing the CH<sub>2</sub> and CH<sub>3</sub> images before subtraction. Linear look-up tables are applied for the RGB coloring. H&E-like colors were applied using the “multiply layers” blend mode in Adobe Photoshop.

### Animal handling and preparation

All animals were treated in compliance with Harvard IACUC protocols #29-01 and #10-02. Mice were euthanized using CO<sub>2</sub> or by an overdose of ketamine and xylazine, followed by cervical spine dislocation. Organs were harvested and imaged immediately. We used a mouse brain matrix (Harvard Apparatus) to produce 1mm thick tissue slices and mounted them stably for imaging between a No.1 coverslip and a coverslide using a ~480µm spacer (Grace Bio-Labs Inc.). For the comparison with H&E-stained micrographs, the brain was coronally sectioned and one half was immediately fixed in 10% formalin for standard histopathological evaluation, while the other was imaged without further preparation as described above. Comparison is shown from mirror-images.

**Invasive glioma models**—We created primary brain glioma models from immunocompromised mice. The human glioma stem cell lines were derived from Brigham and Women's Hospital patients undergoing surgery according to approved protocols. These xenografts were derived from glioblastoma biopsies and implanted. Dissected xenografts were washed in artificial cerebrospinal fluid (CSF) and manually dissociated to single cells. Red blood cells were removed using Lympholyte-M (Cedarlane). The cells were cultured in DMEM/F12 (with L-glutamine, Invitrogen) medium containing glucose (0.3%), penicillin/streptomycin (50µg/ml), Apo-transferrin (0.1mg/ml), Progesterone (20nM), Sodium selenite (30nM), putrescine (60µM), insulin (25µM/ml), sodium bicarbonate (3mM), HEPES (10 mM), 20ng/ml EGF and 20ng/ml FGF. Live cells were counted using a hemocytometer and Trypan blue exclusion. The Brigham and Women's Hospital IACUC protocol number is 000995.

**Metastasis model**—We created breast cancer metastasis models from nude mice (Harlan Laboratory). MDA-MB-231 breast cancer cells were cultured in Eagle's Minimum Essential Medium (ATCC, containing non-essential amino acids, 2mM L-glutamine, 1mM sodium pyruvate, and 1500mg/L sodium bicarbonate) supplemented with 10% fetal bovine serum, 1% penicillin-streptomycin, and grown in a 5% CO<sub>2</sub> incubator at 37°C. Metastatic breast cancer were established by intracranially injecting 1×10<sup>5</sup> MDA-MB-231 cells (in 2µl PBS) at 1mm posterior to bregma, lateral 2mm and 2.5mm depth from skull surface. The Brigham and Women's Hospital IACUC protocol number is 04662.

**Stroke model**—We used a transient model of focal brain ischemia in C57/BL6J mice (Charles River lab). Under an operating microscope (Leica), the origin of right common carotid artery (CCA) was ligated with 6-0 silk suture. A loose ligature and a microvascular clip (F.S.T) were placed on the CCA before the origin of the internal carotid artery (ICA). An incision was made between the two sutures through which the silicone coated tip (HeraeusKulzer) of a 7-0 filament was advanced to the origin of the middle cerebral artery (MCA). With a flexible fiber probe fixed to the right skull above the MCA, regional cerebral

blood flow was monitored with laser Doppler flowmetry (PF2B, Perimed) to confirm successful MCA occlusion and reperfusion. The filament was withdrawn 30 minutes later. Mice were euthanized at day 3 post-ischemia. The Massachusetts General Hospital IACUC protocol number is 2007N000168.

**EAE induction model**—We created relapsing-remitting EAE (R-EAE) from C57Bl/6 mice (Charles-River). Each mouse was immunized subcutaneously (into the flanks) with 100 $\mu$ g of MOG35-55 (MEVGWYRSPFSRVVHLYRNGK), 400 $\mu$ g of Mycobacterium tuberculosis (strain H37Ra; Difco) in complete Freund's adjuvant (CFA, Difco). 100ng of Bordetella pertussis toxin (List Biological Laboratories via Cedarlane Ltd.) was given intravenously at the time of immunization and 2 days later. The Brigham and Women's Hospital IACUC protocol number is 04576.

## Results

### Mechanism of Multicolor Image Contrast

Different molecules in the sample can be selectively imaged by tuning the difference frequency of the excitation beams into the target vibrational resonance (see Methods). Fig. 1A shows the vibrational spectra of the three major components of cells and tissue (lipids, protein and water) with characteristic peaks for the CH<sub>2</sub> and CH<sub>3</sub> stretching vibrations at 2845cm<sup>-1</sup> and 2940cm<sup>-1</sup>, respectively. While imaging of DNA and RNA has recently been demonstrated with CRI in the finger-print region of Raman spectra<sup>26</sup>, the above 3 species are present in higher concentration and allow for faster imaging speed, as desirable for medical *in vivo* imaging<sup>18</sup>.

Figs. 1B-D show SRS images of a C2C12 mammalian cell at these two bands. Consistent with spontaneous Raman spectroscopy<sup>27</sup>, the CH<sub>2</sub> image (Fig. 1B) mainly highlights lipids in the cytoplasm, while lipid-poor nuclei appear dark and featureless. The CH<sub>3</sub> image (Fig. 1C) shows signal from both lipids and proteins (Fig. 1A). The same cytoplasmic features can be seen as in the CH<sub>2</sub> image, but there is additional detail from within nuclei. We have demonstrated that a quantitative protein image<sup>17</sup>, which shows a similar distribution of proteins in both the nucleus and cytoplasm, can be extracted from the CH<sub>2</sub> and CH<sub>3</sub> images based on the Raman ratios in Fig. 1A. Here we aim to generate a vibrational counter-stain to the CH<sub>2</sub> image that accentuates nuclei similarly to hematoxylin component of an H&E stain. To do so, we subtract the CH<sub>2</sub> from the CH<sub>3</sub> image such that the cytoplasmic signal essentially vanishes and then threshold the resulting difference image to only show nuclear signal. This is possible in a robust way because the low CH<sub>2</sub> signal inside the nucleus. Fig. 1D illustrates the resulting multi-color overlay showing the cell-body information from the CH<sub>2</sub> image in green and nuclear information from a thresholded CH<sub>3</sub>-CH<sub>2</sub> difference image in blue. Diagnostically important sub-nuclear features such as nucleoli are visible in the thresholded CH<sub>3</sub>-CH<sub>2</sub> difference image, demonstrating that it is a true nuclear counterstain rather than merely the inverse of the CH<sub>2</sub> image.

Figs. 1E-J illustrate similar contrast obtained in fresh mouse brain tissue. Fig. 1E and the green component of Fig. 1H show the CH<sub>2</sub> signal from lipid-rich myelinated axons<sup>28</sup> and unmyelinated neuropil. Additionally, the vibrationally off-resonant image (Fig. 1G) has

contrast due two-color two-photon absorption (TPA)<sup>9,16,29</sup> and shows individual red blood cells within capillaries due to hemoglobin absorption. Overlaying these three images results in a single three-color, stain-free histological image shown in Fig. 1H. Since the choice of the color scheme is arbitrary, it is possible to choose the look-up tables to mimic an H&E stained section (Fig. 1J). This allows easy comparison with traditional histopathological techniques (Fig. 1I). Comparison of Fig. 1I and J reveals that the stain-free image is free of the vacuolization observed in the H&E stained section because the fresh tissue imaging eliminates the need for freezing, fixation or sections and hence associated tissue processing artifacts.

### Tissue Imaging of Various Organs

To further demonstrate the universal utility of this multi-color contrast we imaged a variety of organs of a wild-type mouse (Fig. 2). The myocardium image (Fig. 2B) shows myocytes with numerous lipid droplets, central nuclei and a rich vascular network. The typical morphology of the renal glomerulus inside Bowman's capsule with tufts of capillaries and surrounding renal tubules is seen in the image of the kidney (Fig. 2C). Variable lipid storage within hepatocytes is seen in the liver (Fig. 2D). In the lung, the vast capillary network of the alveolar walls is highlighted in the red channel (Fig. 2E). Characteristic cross striations and capillaries around the myocytes are easily identified in the skeletal muscle image (Fig. 2F). Clusters of germinal cells and larger blood vessels are seen in the ovary (Fig. 2G). Fig. 2H shows two different layers of mouse skin including the *stratum corneum* layer (top) with a cobblestone arrangement of cells and a protein-rich hair shaft in blue. A deeper image of the epidermis (bottom) collected simply by changing the level of focus highlights many nuclei in the *stratum basale*. The germinal centers with abundant green cytoplasm surrounded by mature lymphocytes with higher nuclear-to-cytoplasmic ratio, as well as scattered red blood cells, are observed in the white pulp of the spleen (Fig. 2I).

### Tissue Imaging of Normal Mouse Nervous System

Imaging of gray matter (Fig. 3A) demonstrates neuronal cell bodies in blue, reflecting a strong signal in the CH<sub>3</sub>-CH<sub>2</sub> channel within a background of the lipid-rich neuropil. Linear processes in green, due to high CH<sub>2</sub> signal, are axons (Figs. 3A to E). The white matter from the *corpus callosum* is dominated by densely packed axons with interspersed oligodendrocytes (Fig. 3E). The cytoarchitecture of various regions including the thalamus (B), the dentate gyrus (C) and the granular cell layer of the cerebellar cortex (D) is easily distinguished, as compared with the mirror images stained with Luxol-H&E (Figs. 3F to J)

### Diagnostic Features in Brain Lesions

In addition to demonstrating image quality and histopathological information in healthy tissue, we imaged mouse models of four relatively common brain pathologies including glioblastoma, metastases, demyelination and stroke. We aimed at recognizing tumor from normal tissue, tumor margins, inflammatory infiltration and evidence of demyelination and cell death. For this reason, we imaged mouse models of invasive, high-grade glioma derived from human brain tumor stem cells, and breast cancer metastasis as well as demyelination and stroke models. Fresh tissue samples were bisected to acquire corresponding stain-free

and paraffin-embedded, H&E-stained images from the same region of the same animal (Fig. 4).

In comparison to healthy brain, increased cellularity, a fundamental histopathological feature of neoplasia, is made obvious in SRS and H&E images for both primary brain tumors (Figs. 4A, B, E, and F) and brain metastases (Figs. 4C, D, G, and H). The remaining myelinated axons interspersed between tumor cells are visible in the center of the infiltrating glioma (Fig. 4A) in contrast with the solid, expansile metastatic tumor (Fig. 4C). Images of tumor margins illustrate the diffusely invasive nature of glial cells along white matter tracts of the *corpus callosum* (Fig. 4B), whereas a sharply defined margin is seen between metastasis and adjacent normal brain tissue (Fig. 4D). A three-dimensional image stack of the tumor margin further highlights this critical diagnostic feature (Video S1).

Among other pathologies that can mimic brain cancer on MRI and CT are tumefactive demyelination and subacute stroke<sup>30</sup>. Fig. 5 and Videos S2 and S3 show multicolor SRS images of mouse models of experimental autoimmune encephalitis (EAE) and ischemic stroke. The comparison with corresponding H&E images shows similar diagnostic features. Lipid-laden macrophages and perivascular lymphocytes (Fig. 5A and C) were present in areas of demyelination. Tissue vacuolization due to cerebral edema was seen as black holes (Fig. 5B and D), which correlated well with the presence of clear vacuoles on H&E-stained sections. Foamy macrophages and condensation of nuclei correlated with apoptosis.

## Discussion

We report the successful acquisition of microscopic, multi-colored images of diagnostic quality on various fresh tissues, without the need for tissue fixation, processing or staining. We acquired images of multiple normal mouse organs and compared them with routine histopathology. Recognition of various tissue types of different organs was easy and characteristic histological features were demonstrated with a clarity that approaches that of traditional H&E staining. In addition, all major histologic features demonstrated in H&E-stained sections of cerebral cortex, white matter, diencephalon and cerebellum were visualized with CRI. Given the great variety of histopathological features in various conditions, we also imaged multiple regions of the normal mouse brain as well as models of glioma, metastasis, stroke and demyelination.

The goal of this study was to demonstrate medical utility of CRI stain-free histology using a research type microscope in *ex vivo* tissue to motivate the design of a clinical prototype instrument in the future. We used the original instrumentation of SRS microscopy<sup>4</sup>; The imaging speed was limited by the speed of the commercial lock-in amplifier and signal was collected in sample transmission. Since completion of the data acquisition, we have developed faster detection electronics and an improved signal collection scheme, which enable SRS at video-rate and in reflection from thick tissue samples, and demonstrated SRS *in vivo* imaging<sup>8</sup>. For this study we also used temporal multiplexing to acquire the individual color channels sequentially. Development of real-time multicolor imaging is underway<sup>17,31</sup> and will be available for the clinical prototype. TPA can also be probed at 827nm, so more robust and inexpensive fiber lasers with a limited tuning range over the CH-region of Raman

spectra can be used in future. Because imaging depth in CRS is limited to about 150 microns, the most immediate applications are in imaging exposed tissue such as *ex vivo* pathological samples, skin, and *in vivo* intra operative margins. The development of a fiber-coupled hand-held scanner for intra operative use is underway<sup>22-25</sup>. Imaging of hollow organs inside the living patient will require further development of endoscopic instrumentation in the future.

Other label-free microscopy techniques used for *in situ* stain-free histopathology such as Infrared (IR) absorption microscopy<sup>32</sup> allow multi-color imaging, however the spatial resolution is limited due to the long wavelength used in IR microscopy<sup>21</sup>. Alternative high-resolution techniques include confocal reflection (CR), optical coherence tomography (OCT), two-photon excited auto-fluorescence (TPAF), second harmonic generation (SHG) and third harmonic generation (THG) microscopy<sup>33-37</sup>. They either lack the capability for multi-color, chemical imaging (CF, OCT & THG) or have contrast limited to a few, specific molecules (TPAF & SHG)<sup>38-40</sup>. The latter techniques are more similar to specific functional stains (e.g. antibody stains) in traditional histopathology, which can be used after abnormalities have been recognized on H&E sections. TPAF has also been demonstrated to allow identification of nuclear and cytosolic regions<sup>41,42</sup> because of absence of TPAF signal inside the nucleus, analogous to the dark nuclei seen in the CH<sub>2</sub> CRI scans. Multi-color CRI can additionally provide a “counter-stain” image with positive nuclear contrast for diagnostically important sub-nuclear features, which makes multicolor CRI images an ideal foundation for versatile *in situ* histopathological tissue diagnosis.

In conclusion, we have demonstrated the use of CRI for microscopic tissue imaging in a label-free manner. Moreover, CRI can be used to generate a degree of contrast, based on the intrinsic vibrational spectrum of the molecular components of biologic tissues that exceeds other label-free optical imaging methods. Our data indicates that CRI can be used for generating high quality histological images without the need of routine tissue processing. Additional work will be required to comprehensively compile an atlas of CRI images of normal tissue and various disorders. However, a preliminary sampling of key neurologic diseases supports the diagnostic capability of CRI. Although, technical hurdles in creating practical intraoperative instrumentation remains, these findings reinforce the possibility that CRI can become an invaluable clinical tool for intraoperative distinction of tumor from normal tissue and immediate margin assessment of *in situ* tissue before surgical closure.

## Supplementary Material

Refer to Web version on PubMed Central for supplementary material.

## Acknowledgments

We thank Dr. John Sims for the mouse stroke model, Chrissy Rooney for the invasive glioma model, Dr. Fa-Ke Lu and SrinjanBasu for the cell images, and Dr. Anita Huettner for early pathology work.

**Funding:** C.W.F. and B.G.S. thank Boehringer Ingelheim Fonds for a Ph.D. Fellowship and the Army Research Office for a National Defense Science and Engineering Graduate Fellowship, respectively. L.O. acknowledges the Italian Society of Multiple Sclerosis (FISM, Cod 2008/B/5). P.L.D. is a Harry Weaver neuroscience scholar of the National Multiple Sclerosis society and C.W. acknowledges NIH (R01NS049263). This work was supported by the NIH Director's Pioneer Award (to X.S.X.) and NIH/NIBIB T-R01 (grant 1R01EB010244-01).

## References

1. Zumbusch A, Holtom GR, Xie XS. Three-dimensional vibrational imaging by coherent anti-Stokes Raman scattering. *Phys Rev Lett*. 1999; 82:4142–4145.
2. Evans CL, Xie XS. Coherent anti-Stokes Raman scattering microscopy: Chemical imaging for biology and medicine. *Annu Rev Anal Chem*. 2008; 1:27.
3. Ploetz E, Laimgruber S, Berner S, Zinth W, Gilch P. Femtosecond stimulated Raman microscopy. *Appl Phys B*. 2007; 87:389–393.
4. Freudiger CW, et al. Label-free biomedical imaging with high sensitivity by stimulated Raman scattering microscopy. *Science*. 2008; 322:1857–1861. [PubMed: 19095943]
5. Ozeki Y, Dake F, Kajiyama S, Fukui K, Itoh K. Analysis and experimental assessment of the sensitivity of stimulated Raman scattering microscopy. *Optics Express*. 2009; 17:3651–3658. [PubMed: 19259205]
6. Nandakumar P, Kovalev A, Volkmer A. Vibrational imaging based on stimulated Raman scattering microscopy. *New Journal of Physics*. 2009; 11
7. Evans CL, et al. Chemical imaging of tissue *in vivo* with video-rate coherent anti-Stokes Raman scattering microscopy. *Proceedings of the National Academy of Sciences of the United States of America*. 2005; 102:16807–16812. [PubMed: 16263923]
8. Saar BG, et al. Video-rate molecular imaging *in vivo* with stimulated Raman scattering. *Science*. 2010; 330:1368–1370. [PubMed: 21127249]
9. Fu D, Ye T, Matthews TE, Yurtsever G, Warren WS. Two-color, two-photon, and excited-state absorption microscopy. *Journal of Biomedical Optics*. 2007; 12:54004–54009.
10. Cheng JX, Volkmer A, Book LD, Xie XS. An epi-detected coherent anti-Stokes Raman scattering (E-CARS) microscope with high spectral resolution and high sensitivity. *Journal of Physical Chemistry B*. 2001; 105:1277–1280. [10.1021/Jp003774a](https://doi.org/10.1021/Jp003774a)
11. Nan XL, Potma EO, Xie XS. Nonperturbative chemical imaging of organelle transport in living cells with coherent anti-Stokes Raman scattering microscopy. *Biophysical Journal*. 2006; 91:728–735.
12. Fu Y, Wang HF, Shi RY, Cheng JX. Characterization of photodamage in coherent anti-Stokes Raman scattering microscopy. *Optics Express*. 2006; 14:3942–3951. [PubMed: 19516542]
13. Fu Y, Wang HF, Huff TB, Shi R, Cheng JX. Coherent anti-Stokes Raman scattering imaging of myelin degradation reveals a calcium-dependent pathway in lyso-PtdCho-induced demyelination. *Journal of Neuroscience Research*. 2007; 85:2870–2881. [PubMed: 17551984]
14. Fu Y, Huff TB, Wang HW, Wang HF, Cheng JX. *Ex vivo* and *in vivo* imaging of myelin fibers in mouse brain by coherent anti-Stokes Raman scattering microscopy. *Optics Express*. 2008; 16:19396–19409. [PubMed: 19030027]
15. Henry FP, et al. Real-Time *in vivo* assessment of the nerve microenvironment with coherent anti-Stokes Raman scattering microscopy. *Plastic and Reconstructive Surgery*. 2009; 123:123s–130s. [PubMed: 19182671]
16. Fu D, et al. High-resolution *in vivo* imaging of blood vessels without labeling. *Opt Lett*. 2007; 32:2641–2643. [PubMed: 17873920]
17. Fu D, et al. Quantitative chemical imaging with multiplex stimulated Raman scattering microscopy. *Journal of the American Chemical Society*. 2012
18. Evans CL, et al. Chemically-selective imaging of brain structures with CARS microscopy. *Optics Express*. 2007; 15:12076–12087. [PubMed: 19547572]
19. Begin S, Belanger E, Laffray S, Vallee R, Côté D. *In vivo* optical monitoring of tissue pathologies and diseases with vibrational contrast. *Journal of Biophotonics*. 2009; 2:632–642. [PubMed: 19847801]
20. Chowdary PD, et al. Molecular histopathology by spectrally reconstructed nonlinear interferometric vibrational imaging. *Cancer Res*. 2010; 70:9562–9569. [10.1158/0008-5472.Can-10-1554](https://doi.org/10.1158/0008-5472.Can-10-1554) [PubMed: 21098699]
21. Meyer T, et al. Nonlinear microscopy, infrared, and Raman microspectroscopy for brain tumor analysis (Journal Paper). *Journal of Biomedical Optics*. 2011; 16:021113. [PubMed: 21361676]

22. Légaré F, Evans CL, Ganikhanov F, Xie XS. Towards CARS endoscopy. *Opt Express*. 2006; 14:4427–4432. [PubMed: 19516594]
23. Murugkar S, et al. Miniaturized multimodal CARS microscope based on MEMS scanning and a single laser source. *Optics Express*. 2010; 18:23796–23804. [PubMed: 21164724]
24. Balu M, Liu G, Chen Z, Tromberg BJ, Potma EO. Fiber delivered probe for efficient CARS imaging of tissues. *Optics Express*. 2010; 18:2380–2388. [PubMed: 20174068]
25. Saar BG, Johnston RS, Freudiger CW, Xie XS, Seibel EJ. Coherent Raman scanning fiber endoscopy. *Optics Letters*. 2011; 36:2396–2398. [PubMed: 21725423]
26. Zhang X, et al. Label-free live-cell imaging of nucleic acids using stimulated Raman scattering microscopy. *ChemPhysChem*. 2012
27. Slipchenko MN, Le TT, Chen HT, Cheng JX. High-speed vibrational imaging and spectral analysis of lipid bodies by compound Raman microscopy. *Journal of Physical Chemistry B*. 2009; 113:7681–7686.
28. Wang HF, Fu Y, Zickmund P, Shi RY, Cheng JX. Coherent anti-stokes Raman scattering imaging of axonal myelin in live spinal tissues. *Biophysical Journal*. 2005; 89:581–591. [PubMed: 15834003]
29. Matthews TE, Piletic IR, Selim MA, Simpson MJ, Warren WS. Pump-probe imaging differentiates melanoma from melanocytic nevi. *Science Translational Medicine*. 2011; 3:71ra15.
30. Omuro AMP, Leite CC, Mokhtari K, Delattre JY. Pitfalls in the diagnosis of brain tumours. *Lancet Neurology*. 2006; 5:937–948. [PubMed: 17052661]
31. Laffray S, et al. Adaptive movement compensation for *in vivo* imaging of fast cellular dynamics within a moving tissue. *PloS one*. 2011; 6:e19928. [PubMed: 21629702]
32. Gremlich, HU.; Yan, B. Infrared and Raman spectroscopy of biological materials. Vol. 24. CRC; 2001.
33. Master, BR.; So, PTC. Biomedical nonlinear optical microscopy. Oxford University Press; 2008.
34. König K, et al. Clinical two-photon microendoscopy. *Microscopy Research and Technique*. 2007; 70:398–402. [PubMed: 17393493]
35. Tearney GJ, et al. In vivo endoscopic optical biopsy with optical coherence tomography. *Science*. 1997; 276:2037–2039. [PubMed: 9197265]
36. Tai S, et al. Optical biopsy of fixed human skin with backward-collected optical harmonics signals. *Optics Express*. 2005; 13:8231–8242. [PubMed: 19498853]
37. Witte S, et al. Label-free live brain imaging and targeted patching with third-harmonic generation microscopy. *Proceedings of the National Academy of Sciences*. 2011; 108:5970.
38. Zipfel WR, et al. Live tissue intrinsic emission microscopy using multiphoton-excited native fluorescence and second harmonic generation. *Proceedings of the National Academy of Sciences of the United States of America*. 2003; 100:7075–7080. [PubMed: 12756303]
39. Li CQ, et al. Imaging leukocyte trafficking in vivo with two-photon-excited endogenous tryptophan fluorescence. *Optics Express*. 2010; 18:988–999. [PubMed: 20173920]
40. Campagnola PJ, et al. Three-dimensional high-resolution second-harmonic generation imaging of endogenous structural proteins in biological tissues. *Biophysical Journal*. 2002; 82:493–508. [PubMed: 11751336]
41. Palero JA, de Bruijn HS, van der Ploeg van den Heuvel A, Sterenborg HJCM, Gerritsen HC. Spectrally resolved multiphoton imaging of *in vivo* and excised mouse skin tissues. *Biophysical journal*. 2007; 93:992–1007. [PubMed: 17449667]
42. König K. Clinical multiphoton tomography. *Journal of biophotonics*. 2008; 1:13–23. [PubMed: 19343631]

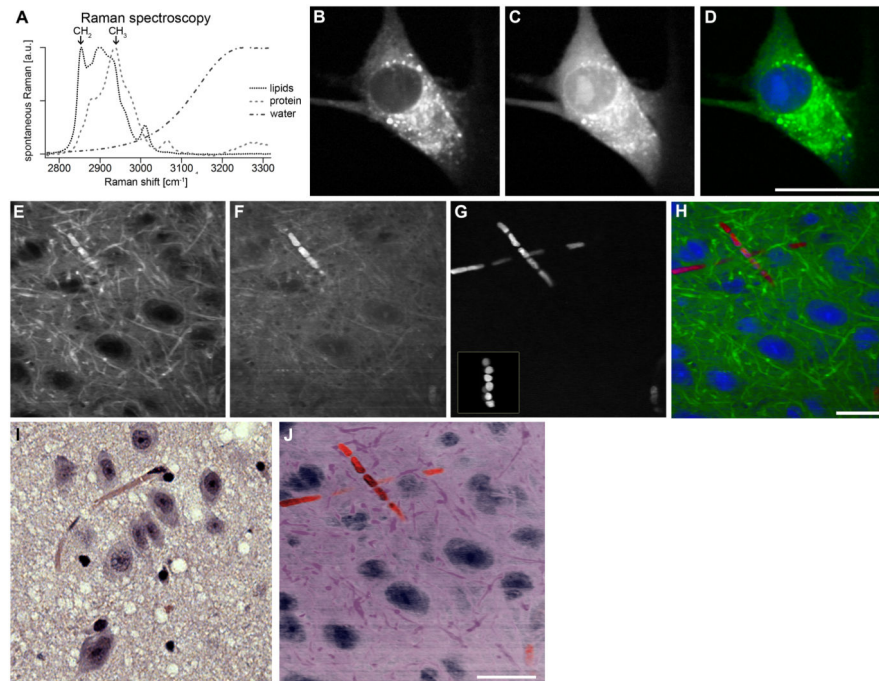


**Figure 1.**

Stain-free histologic imaging with multi-color CRI. (A) Vibrational spectra of the major constituents of tissue: lipids, protein and water. Arrows indicate Raman shifts at which imaging is performed. (B-D) SRS images of a live C2C12 mammalian cell acquired at the CH<sub>2</sub>-stretching vibration at 2845cm<sup>-1</sup>(B) and CH<sub>3</sub>-stretching vibration at 2940cm<sup>-1</sup> (C). Multicolor image (D) generated from images (B) and (C) with the green channel (CH<sub>2</sub> image) showing the cell-body and the blue channel (thresholded CH<sub>3</sub>-CH<sub>2</sub> difference image) highlighting the nuclear morphology including a bright nucleolus. (E-H) SRS images of fresh *ex vivo* brain tissue acquired at CH<sub>2</sub>-stretching vibration at 2845cm<sup>-1</sup> (E), CH<sub>3</sub>-stretching vibration at 2940cm<sup>-1</sup> (F), and vibrationally off-resonant showing TPA of hemoglobin at a sum frequency of 23,700 cm<sup>-1</sup> (G). Multicolor image (H) generated from images (E-G) with the green channel (CH<sub>2</sub> image) highlighting cytoplasm and myelin sheaths, blue channel (thresholded CH<sub>3</sub>-CH<sub>2</sub> difference image) showing the nuclear morphology, and the red channel (hemoglobin image) highlighting red blood cells. (I) H&E-stained micrograph from the same region in the brain. (J) Same multicolor image as (H) with a different pseudo-color scheme, chosen to mimic the appearance of an H&E-stained micrograph, illustrates the similar image content and appearance of stain-free images and H&E stained sections. Scale bar, 25 μm.

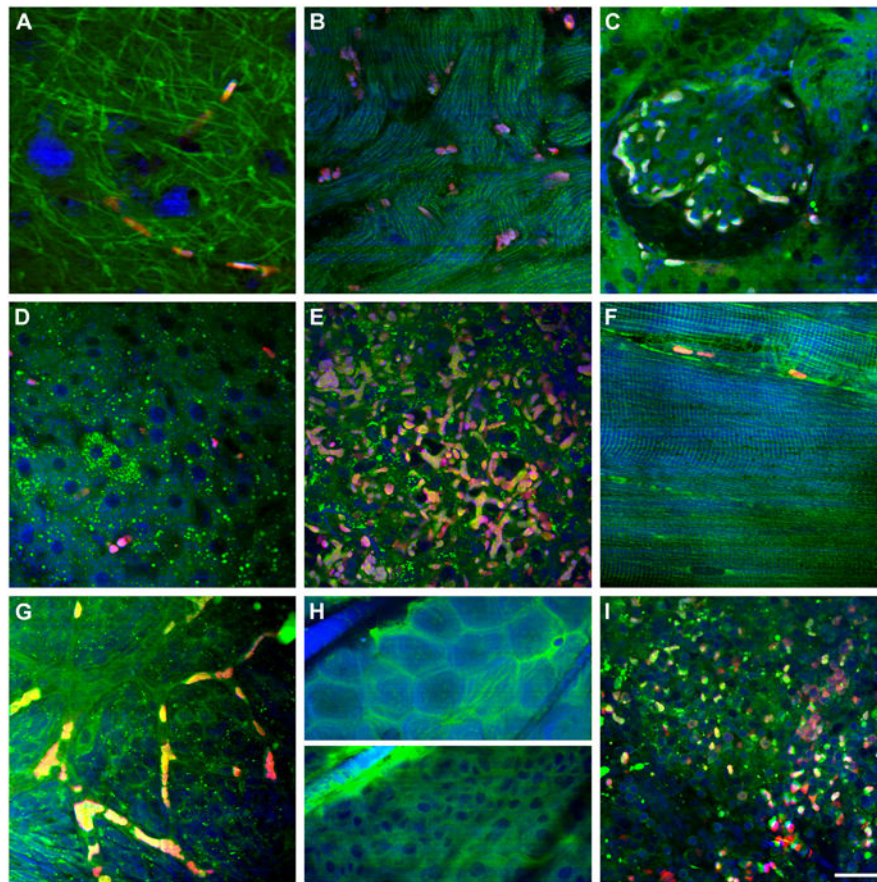


**Figure 2.** Multicolor stain-free images of various mouse organs (green: CH<sub>2</sub> image; blue: CH<sub>3</sub>-CH<sub>2</sub> difference image; red: hemoglobin image) of (A) brain, (B) heart, (C) kidney, (D) liver, (E) lung, (F) muscle, (G) ovary, (H) skin with *stratum corneum* (top) and *stratum basale* (bottom) and (I) spleen. Scale bar, 25  $\mu$ m.

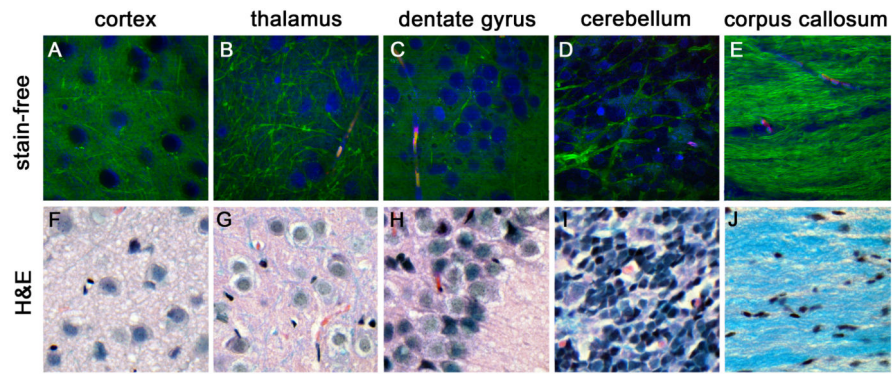


**Figure 3.** Multicolor stain-free images of various brain regions in a wild-type mouse in comparison with paraffin-embedded, H&E and Luxol-stained sections. (green: CH<sub>2</sub> image; blue: CH<sub>3</sub>-CH<sub>2</sub> difference image; red: hemoglobin image) of (A) cortex, (B) thalamus, (C) dentate gyrus, (D) cerebellum, and (E) corpus callosum. (F-J) show H&E/luxol stained section of corresponding regions.

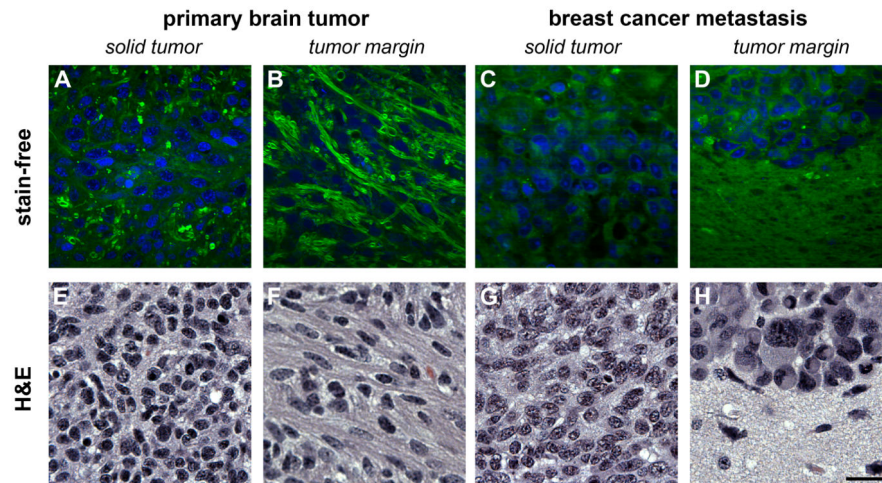


**Figure 4.**

Comparison of multicolor, label-free images with H&E-stained sections of primary mouse models of glioma and metastatic breast cancer. Images display practically identical diagnostic features as visualized with SRS. (A-D) Two-color SRS images (green: CH<sub>2</sub> image; blue: CH<sub>3</sub>-CH<sub>2</sub> difference image) and (E-H) H&E stained micrographs from the same region of the same animal. (A, B, E and F) are acquired from mouse models of primary brain tumor and (C, D, G and H) from models of breast cancer brain metastasis. Hypercellularity is noticeable in both primary tumor and metastasis. The primary brain tumor morphology (A and E) shows residual interspersed axons (highlighted in green), while metastasis (C and G) lacks this feature due to their epithelioid, cohesive and less infiltrative character. Primary and secondary tumors can be further distinguished at the tumor margin, where primary tumor cells invade the healthy tissue (B and F) while metastases produce a sharp margin at the interphase of tumor and normal tissue (D and H). Scale bar, 25 μm.

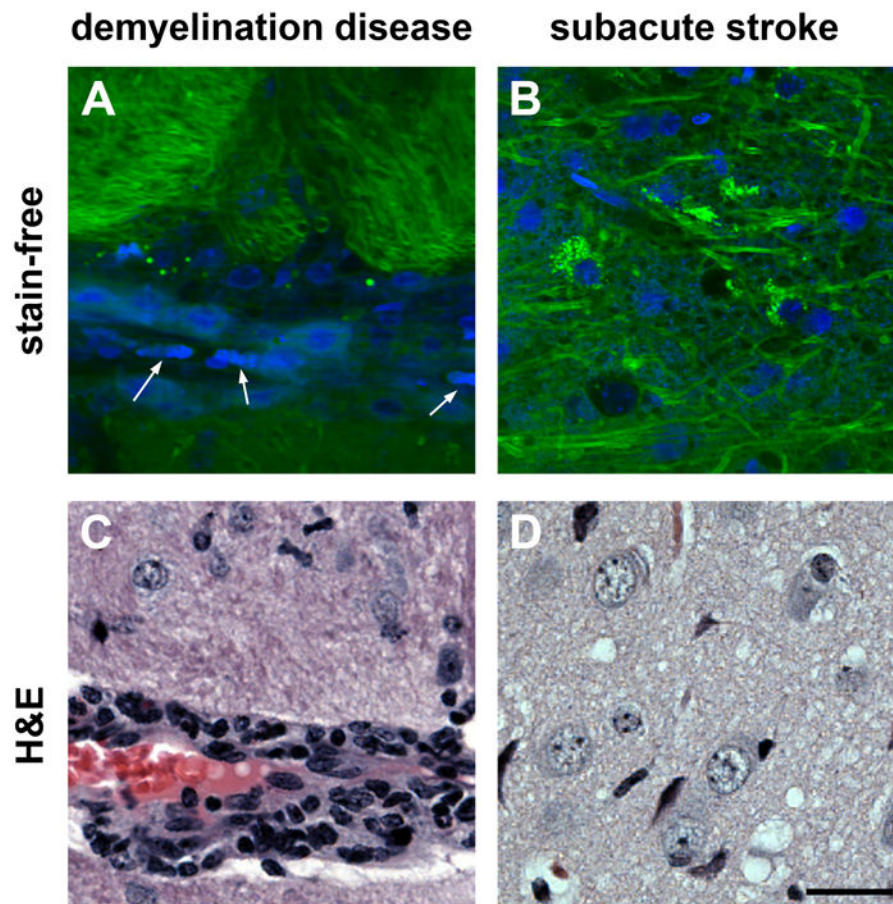


**Figure 5.** SRS label-free images of demyelination and stroke mouse models. **(A)** Two-color SRS image (green:  $\text{CH}_2$  image; blue:  $\text{CH}_3\text{-CH}_2$  difference image) of a demyelinating lesion in a mouse with experimental allergic encephalomyelitis (EAE). **(A)** Perivascular inflammatory cells and histiocytes with large lipid droplets from phagocytized myelin are visible. Red blood cells in a capillary are highlighted by arrows (Hemoglobin image, red, not used in this picture). **(B)** Two-color SRS image of brain tissue in a mouse stroke model three days post-stroke. Macrophages with many small lipid droplets are dispersed throughout the tissue. Dark areas represent edema fluid. **(C,D)** H&E stained micrographs of **(C)** EAE and **(D)** stroke model from the same region. Scale bar, 25  $\mu\text{m}$ .